AIP | Journal of Applied Physics

Effect of dielectric barrier discharge plasma actuators on non-equilibrium hypersonic flows

Ankush Bhatia, Subrata Roy, and Ryan Gosse

Citation: Journal of Applied Physics **116**, 164904 (2014); doi: 10.1063/1.4898862
View online: http://dx.doi.org/10.1063/1.4898862
View Table of Contents: http://scitation.aip.org/content/aip/journal/jap/116/16?ver=pdfcov
Published by the AIP Publishing

JOURNAL OF APPLIED PHYSICS 116, 164904 (2014)

Effect of dielectric barrier discharge plasma actuators on non-equilibrium hypersonic flows

Ankush Bhatia,[1] Subrata Roy,[1] and Ryan Gosse[2]
[1]*Applied Physics Research Group, Department of Mechanical and Aerospace Engineering, University of Florida, Gainesville 32611, USA*
[2]*Computational Sciences Center of Excellence, Air Force Research Laboratory, AFRL/RQHV, Bldg 146B, 2210 Eighth St., WPAFB, Ohio 45433-7512, USA*

(Received 22 June 2014; accepted 9 October 2014; published online 28 October 2014)

A numerical study employing discontinuous Galerkin method demonstrating net surface heat reduction for a cylindrical body in Mach 17 hypersonic flow is presented. This application focuses on using sinusoidal dielectric barrier discharge plasma actuators to inject momentum near the stagnation point. A 5 species finite rate air chemistry model completes the picture by analyzing the effect of the actuator on the flow chemistry. With low velocity near the stagnation point, the plasma actuator sufficiently modifies the fluid momentum. This results in redistribution of the integrated surface heating load on the body. Specifically, a particular configuration of normally pinching plasma actuation is predicted to reduce the surface heat flux at the stagnation point. An average reduction of 0.246% for the integrated and a maximum reduction of 7.68% are reported for the surface heat flux. The temperature contours in the fluid flow (with maximum temperature over 12 000 K) are pinched away from the stagnation point, thus resulting in reduced thermal load. Plasma actuation in this configuration also affects the species concentration distribution near the wall, in addition to the temperature gradient. The combined effect of both, thus results in an average reduction of 0.0986% and a maximum reduction of 4.04% for non-equilibrium calculations. Thus, this study successfully demonstrates the impact of sinusoidal dielectric barrier discharge plasma actuation on the reduction of thermal load on a hypersonic body. © *2014 AIP Publishing LLC*. [http://dx.doi.org/10.1063/1.4898862]

I. INTRODUCTION

Active flow control is a topic of great interest due to its vast practical applications. Amongst various flow control methods, plasma devices have many positive characteristics.[1] They have been applied from subsonic to supersonic to hypersonic flow regimes. Specifically, extensive studies have focused on plasma control of subsonic flows.[2–7] A good amount of work has also been done in the supersonic and hypersonic regimes[8–19] with the aim of reducing net mechanical and thermal loads on the vehicle. However, flow control methods at higher speeds have significant energy budget penalty. As an alternative, we propose the use of microsecond pulsed Dielectric Barrier Discharge (DBD) plasma actuator[7,20–23] for the net reduction of thermal load on a space vehicle in hypersonic re-entry, with relatively lower amount of power requirement.

Plasma actuators have many advantages including design simplicity, rapid response, and lack of moving components, surface compliance, and possibility of application to the most receptive location, relatively low power budget, and robustness.[24] They can be categorized into non-thermal and thermal plasmas. Non-thermal plasmas are known to induce reasonable air flow speeds of 1–10 m/s within a millimeter height from the wall in quiescent flow conditions. Thus, they provide effective control for free stream velocities ranging from low subsonic to supersonic flows.[24–26] Additionally, they have low energy costs, since majority of the electric energy goes into the kinetic energy of the electrons rather than heating of the surrounding gas.[24] The examples of these include corona discharge and micro-second DBD plasma actuators. Thermal plasmas are primarily used for flow control from transonic to supersonic to hypersonic flow regimes, and include counter-flow plasma jets, energy deposition methods using high energy beams like electron and micro-wave, and gas heating using arc or electric discharge between electrodes at the vehicle surface. Thermal plasmas have been reported to provide net drag and surface heat transfer reduction by affecting the shock thickness and speed. Both the widening of the shock and the increase of its standoff distance from the vehicle, results in the weakening of the shock intensity, thus reducing the drag and surface heat transfer to the vehicle. It is a requirement for such mechanisms to have energy efficiency above unity. Despite reported success, the energy budget of this approach remains high (few KWs or higher[10]). Though the cited time averaged power requirement maybe few hundred watts,[24] the instantaneous power requirement may exceed few kilowatts[8,9,12] to even megawatts.[10,27]

DBD plasma actuators have been implemented in nanosecond and microsecond pulse widths. Nanosecond pulsed DBD plasma actuators have also been successful in high speed flow manipulation. As an example, a series of high voltage nanosecond pulses producing rapid localized heating are used to reattach the flow for Mach 0.85 in Ref. 28. In quiescent flow, this nanosecond pulsed DBD plasma actuator is also known to produce shock waves. These compression waves result in a 20% increase in shock stand-off distance of a Mach 5 flow over a cylinder.[10] However, the advantage of heat loss due to the increased shock distance is seen to be compensated by the net heat added. In fact, the profiles for Stanton number, C_h, increased by two orders of magnitude. Therefore, nanosecond pulsed actuation, though promising for increasing the shock stand-off distance, seems to add more heat during its duty cycle. This is detrimental to the re-entry vehicle. As an alternative, we aim to explore the effect of micro-second pulsed DBD plasma to re-entry vehicle, due to its low power requirement.

According to Ref. 29, micro-second pulsed DBD plasma actuators are most effective at bifurcation points in the flow field, to excite the instability modes. Their applications are limited to the flow velocities up to 60 m/s. For hypersonic flow over a cylinder, the flow velocities are very low close to the stagnation point. Thus, it allows us to use micro-second DBD plasma actuators, where the main mechanism is momentum addition through a plasma body force[20] to a flow at low velocity (<=50 m/s). This significantly affects the net heat transfer to the surface of the re-entry vehicle at the stagnation point by locally manipulating the flow. In addition, the power requirement for this device is also low, making the powering scheme less complicated.

This paper is organized as follows. Section II provides the governing equations for Navier Stokes equations for a single species and multiple species relevant for hypersonic flows with and without full thermo-chemical non-equilibrium. Section III discusses the standard plasma DBD actuator and the formulation of the body force. Section IV describes numerical methodology of our in-house discontinuous Galerkin (DG) based multi-scale ionized gas (MIG) flow code, used for simulating the problems presented in this paper. Problem description and boundary conditions for hypersonic flow problem over a cylinder, both with and without thermo-chemistry, is presented in Sec. V. Section VI presents results for hypersonic flows without thermo-chemistry for three configurations used for plasma actuators. Section VII summarizes the findings for hypersonic flows with full non-equilibrium flow chemistry. The baseline cases are compared to other published numerical results. Based on these studies, the most receptive actuator configuration for thermal heat flux control is documented. Finally, conclusions are made about the key findings and future directions.

II. GOVERNING EQUATIONS

We consider hypersonic flows both with and without thermo-chemistry. The governing equations can be written as

$$\frac{\partial U}{\partial t} + \nabla \cdot F_{\mathrm{i}} = \nabla \cdot F_{\mathrm{v}}. \tag{1}$$

Here, the solution variable, U and the inviscid and viscous flux terms, i.e., F_{i} and F_{v}, respectively, are given

$$U = \begin{bmatrix} \rho \\ \rho u \\ \rho v \\ \rho E \end{bmatrix}; \quad F_i^x = \begin{bmatrix} \rho u \\ \rho u^2 + P \\ \rho u v \\ u(\rho E + P) \end{bmatrix}; \quad F_i^y = \begin{bmatrix} \rho v \\ \rho u v \\ \rho v^2 + P \\ v(\rho E + P) \end{bmatrix};$$
$$F_v^x = \begin{bmatrix} 0 \\ \tau_{xx} \\ \tau_{xy} \\ u\tau_{xx} + v\tau_{xy} + q_x \end{bmatrix}; \quad F_v^y = \begin{bmatrix} 0 \\ \tau_{yx} \\ \tau_{yy} \\ u\tau_{yx} + v\tau_{yy} + q_y \end{bmatrix}; \tag{2}$$

where ρ is the gas density, u and v are x- and y-velocities, E is the total energy, P is the pressure, and τ and q are shear stress and the conduction heat flux. For hypersonic flows with thermo-chemistry, we use multi-species Navier Stokes equation. A general form of this equation is written as

$$\frac{\partial U}{\partial t} + \nabla . F_{\mathrm{i}} = \nabla . F_{\mathrm{v}} + G. \tag{3}$$

The solution vector, U, the inviscid and viscous flux terms, F_i and F_v and the source term, G (in Eq. (3)) are given in Eq. (4). ρ_s is the species density, with s = 1, 2,…, 5 for 5 species model of O_2, NO, N, O, and N_2. ρ is the total density, which is the sum of all species density. $\rho\vec{u}$ is the momentum (consisting of both x and y components), ρe_t and ρe_v are the total and vibrational energy, respectively. ρe_t is the sum of the vibrational internal energy, translational-rotational internal energy, kinetic energy and the heat of formation of the present species (Eq. (5)). h_t is the total enthalpy, given by the sum of specific internal energy plus pressure (Eq. (6))

$$U = \begin{bmatrix} \rho_s \\ \rho\vec{u} \\ \rho e_t \\ \rho e_v \end{bmatrix}; \quad \vec{F}_i = \begin{bmatrix} \rho_s \vec{u} \\ \rho\vec{u} \otimes \vec{u} + P \\ \rho\vec{u} h_t \\ \rho\vec{u} h_v \end{bmatrix};$$
$$\vec{F}_{\mathrm{v}} = \begin{bmatrix} -\rho_s \tilde{V}_s \\ \underline{\tau} \\ \underline{\tau}.\vec{u} - \vec{q} - \vec{q}_{\mathrm{v}} - \sum_s h_{t,s}\rho_s \tilde{V}_s \\ -\vec{q}_{\mathrm{v}} - \sum_s h_{v,s}\rho_s \tilde{V}_s \end{bmatrix};$$
$$G = \begin{bmatrix} \omega_s \\ 0 \\ 0 \\ \sum_s \omega_s \hat{e}_{v,s} + Q_{TV} \end{bmatrix}; \tag{4}$$

$$\rho e_t = \rho e_v + \sum_s \rho_s C_{V,tr} T + \sum_s \rho_s h_s^0 + \frac{1}{2}\rho(u^2 + v^2), \tag{5}$$

$$h_t = e_t + \frac{P}{\rho}, \tag{6}$$

where h_v is equal to e_v, since there is no pressure term in the vibrational energy equation, as the kinetic energy is considered only in the total energy equation. $\tilde{V}_s$, appearing in the viscous flux term for the continuity equation for 5 species densities, is the diffusion velocity of the species and is assumed to follow Fick's law:

$$\rho_s \tilde{V}_s = -\rho D_s \nabla c_s. \tag{7}$$

Shear stress, $\underline{\tau}$, and heat fluxes, $\vec{q}$ and $\vec{q}_v$, for translational-rotational modes and vibrational-electronic modes, respectively, are given by

$$\underline{\tau} = \mu(\nabla\vec{u} + \vec{u}\nabla) - \frac{2}{3}\mu\nabla\cdot\vec{u}I,$$
$$\vec{q} = -k\nabla T,$$
$$\vec{q}_{\mathrm{v}} = -k\nabla T_{\mathrm{v}}. \tag{8}$$

Multi-component diffusion coefficient, D_s, is found using Lewis number, Le of 1.4. Viscosity, μ, is found using Wilke's semi-empirical mixing rule,[30] and species viscosities are found using Blottner's model.[31] Conductivities, k and k_v are determined from an Eucken relation.[32] The terms, $\sum_s h_{t,s}\rho_s\tilde{V}_s$ and $\sum_s h_{v,s}\rho_s\tilde{V}_s$ in Eq. (4) in the viscous flux term, denote the transport of total and vibrational energies, respectively, due to mass diffusion of the different species present. Finally, ω_s is the production rate of the different species, due to the chemical reactions identified in Eq. (9). The chemistry source terms are based on a model proposed by Ref. 33. The first three reactions are the dissociation reactions of N_2, O_2, and NO. Here, M is the third body that can be any of the 5 species present, colliding with the dissociating molecule

$$N_2 + M \leftrightarrow N + N + M$$
$$O_2 + M \leftrightarrow O + O + M$$
$$NO + M \leftrightarrow N + O + M$$
$$N_2 + O \leftrightarrow NO + N$$
$$NO + O \leftrightarrow O_2 + N. \tag{9}$$

The last two reactions in Eq. (9) are the exchange reactions, resulting in the oxidation of N_2 and NO species, and production of the atomic nitrogen. $\sum_s \omega_s \hat{e}_{v,s}$ and Q_{TV} in the source term, G in Eq. (4) are, respectively, the production/destruction of the vibrational energy (due to production/destruction of species) and the energy exchange between translational-rotational and vibrational modes. Landau-Teller model is used for Q_{TV}, where the Landau-Teller inter-species relaxation time is given in Ref. 34. The energy first transfers from kinetic to the internal translational-rotational modes, causing a rise in their temperature as the flow stagnates in a hypersonic flow. The internal vibrational modes will then equilibrate with the other modes based on the modeled time scales that are a function of temperature and pressure. Further relevant details about this model can found from Ref. 35.

III. MICRO-SECOND PULSED DBD PLASMA ACTUATORS

DBD plasma actuators have been used for many flow control applications at subsonic Mach numbers.[36–41] The actuator consists of two horizontally displaced electrodes separated by a dielectric material. The powered electrode is typically exposed to the surrounding gas, and the grounded electrode embedded beneath the dielectric. Application of high sinusoidal voltage with a frequency of 1–50 kHz and amplitude of 5–60 kV_{pp}, results in high electric field near the dielectric surface. This high electric field ionizes the gas next to the electrodes, and the combination of electric field and charged particles induces body force on the fluid next to the wall, generating a wall jet (Fig. 1).

A linear configuration is the standard geometry of a DBD plasma actuator (see schematic in Fig. 1). The body force distribution for the linear geometry plasma actuator was modeled in Ref. 20, using first principles based plasma discharge simulations. The force distribution is given in

$$f_x = \frac{F_{x,0}}{\sqrt{F_{x,0}^2 + F_{y,0}^2}} \times \exp\left(-\left(\frac{(x-x_0)-(y-y_0)}{y-y_0+y_b}\right)^2 - \beta_x(y-y_0)^2\right),$$
$$f_y = \frac{F_{y,0}}{\sqrt{F_{x,0}^2 + F_{y,0}^2}} \times \exp\left(-\left(\frac{(x-x_0)}{y-y_0+y_b}\right)^2 - \beta_y(y-y_0)^2\right). \tag{10}$$

Here, $F_{x,0} = 2.6$, $F_{y,0} = 2.0$, $\beta_x = 7.2 \times 10^4$, $\beta_y = 9 \times 10^5$, and $y_b = 0.00333$. x_0 and y_0 represent the edge location of the electrodes. Though this body force is not as accurate as a fully coupled simulation of the plasma and fluid dynamics, it is more accurate than phenomenological models. This approach also avoids the expensive computations required for fully coupled simulations that include the electro-magnetic field.

The force distribution for the plasma actuator imposed on the cylinder, following Eq. (10), is shown in Fig. 2. Herein, only F_x is shown (here, x is parallel to DBD actuator, and is different from x and y axis shown in the figure). This F_x is multiplied by a factor of 15294 to get a representative integrated value of 40 mN/m, the average body force obtained from plasma DBD actuators. The force distribution is on the flow field in front of the stagnation region, which is exposed to an incoming Mach number of 17.65, in this paper. The actuator applied to this case is also shown in Fig. 2, and it actuates the fluid, next to the stagnation point, in the upward or +y-direction.

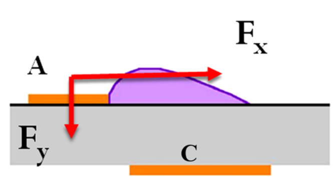

FIG. 1. Schematic of DBD plasma actuator, with exposed electrode (A) and grounded electrode (C). A sinusoidal AC pulse of high potential difference across the exposed and grounded electrodes causes a high electric field near the surface, which causes the air to ionize. This electric field then applies a body force on charged particles near the surface that causes the neutral gas to the left of exposed electrode to be pulled in an induced wall jet.

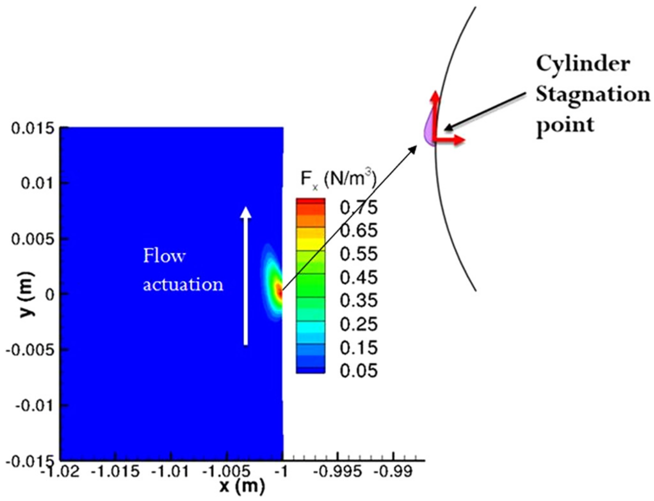

FIG. 2. Force distribution of F_x (acting in the positive y-direction) for plasma actuator applied at the stagnation point of the cylinder.

As can be seen in this figure, the plasma body force is localized at high magnitude. Its predominant effect is concentrated within a region of 3–10 mm about the stagnation point. Since the flow velocities are very low, next to the stagnation point, a significant effect of the plasma actuator on the hypersonic flow is to be expected near the stagnation region.

The applicability of the force model (which is generally applied at STP conditions), given by Eq. (10), at hypersonic flow conditions at the stagnation point of the cylinder is an engineering assumption, and can be justified in the following manner. The flow velocities at the region where plasma body force acts are lower than 15 m/s (see Fig. 14). This velocity regime agrees well with the literature of DBD plasma flow control. The free stream pressure for the given flow is 56 Pa, corresponding to a 50 km re-entry altitude. Corresponding pressure at the stagnation point is 0.227 atm. Based on published report, a stable and homogenous discharge can be obtained for pressures between 10^4 and 10^5 Pa,[42] making this application feasible at the given pressure at the stagnation point. Additionally, low pressure thrust measurements[43,44] also show similar values at 0.227 atm and 1 atm. This justifies the use of the force model for the given pressure conditions at the stagnation point. Finally, the temperature values rise from 500 K (at the wall) to nearly 10750 K and 5250 K (at about 5 mm distance away from the cylinder wall, where the plasma body force is significant, see Figs. 10 and 22, respectively), for hypersonic flows with and without chemistry, respectively. Even though the temperature value is far from STP, the presence of high energy molecules and free radicals (N_2 and O_2 for the case without chemistry and N, O, NO, N_2, and O_2 for the case with chemistry), near the cylinder surface, will only aid the ionization process. Hence, a better performance for the surface heat reduction is to be expected than currently predicted using the plasma DBD force model available in hand. In addition, to ascertain its general applicability, this force model has been validated with physical experiments under quiescent and subsonic flow conditions.[7,45]

IV. NUMERICAL METHODOLOGY

Our in-house MIG solver was used for simulating the problems presented in this work. MIG is a multi-physics finite element based code. It has been used to solve various fluid-plasma interaction problems.[21–23,46] MIG's original formulation is Galerkin based finite element method, which requires the solution to be continuous across the elements' interfaces (Fig. 3). This however limits the application of MIG to diffusion dominated problems. For extending MIG to high-speed flows, a DG framework was incorporated. This was conveniently done owing to MIG's modular structure. Some successful applications of DG method applied to MIG have been presented in Refs. 47, 48, and 35.

The discontinuous Galerkin method is a finite element based method, where in the solution continuity constraint across elements' interfaces is relaxed. This makes DG method suitable for various high-speed flow problems.[49–56] DG methods are known to combine the relative advantages of finite volume method (for convection dominated problems) and finite element methods (for unstructured meshes and complex geometries). In addition, DG method is also a compact stencil high-order accurate method that makes it convenient to extend to higher orders without any extra coding effort.

For basis functions, we use 2D Jacobi polynomials[56] given by

$$P_n^{\alpha,\beta}(x) = \frac{(-1)^n}{2^n n!}(1-x)^{\alpha}(1+x)^{-\beta}\frac{d^n}{dx^n} \times \left\{(1-x)^{\alpha+n}(1+x)^{\beta+n}\right\}. \quad (11)$$

To summarize the DG method used in this work, local Lax-Friedrichs flux[57] and second formulation of Bassi and Rebay, namely, BR2 scheme[58] are used for the inviscid and viscous numerical fluxes, which are defined at the element interfaces. Backward Euler, an implicit time integration method, is used for advancement of solution with high Courant-Friedrichs-Lewy, CFL numbers (approximately 5000).

To capture the shock, we use r-p adaptivity method proposed and presented in Refs. 35 and 48. In this approach, we use pressure based shock sensors[54] (Eq. (12)) to clearly identify the shock location

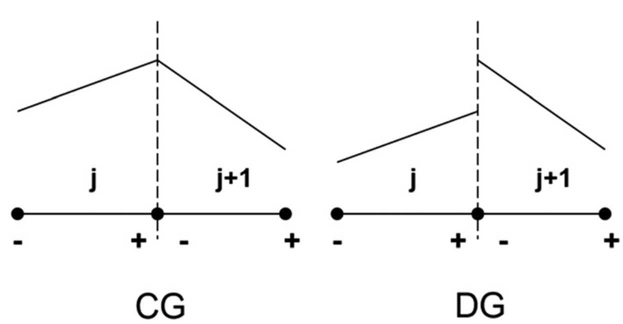

FIG. 3. Schematic showing solution variation across two neighboring elements in continuous Galerkin (CG) and DG. Solution across neighboring elements is required to be continuous in CG and allowed to be discontinuous in DG.

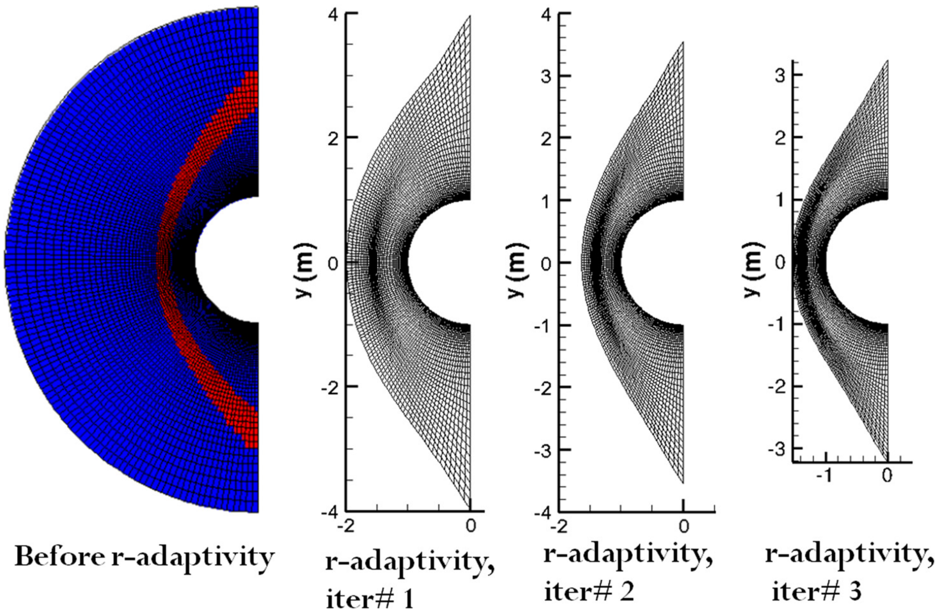

FIG. 4. Mesh resolution using r-p adaptivity iterations. (a) Mesh before r-p adaptivity. Elements in the shock are identified in red and element outside the shock are identified in blue. (b) Mesh after first r-p adaptivity iteration. Elements outside the shock are moved to within the shock to refine the elements in the shock. (c) Second r-p adaptivity iteration and (d) third r-p adaptivity iteration. Shock mesh resolution is successively improved with each iteration of r-p adaptivity, without increasing the total number of elements.

$$s_k = \log_{10}\left(\frac{1}{|\partial\Omega_k|}\int_{\partial\Omega_k}\left|\frac{[P_h].\vec{n}}{\{P_h\}}\right|ds\right). \tag{12}$$

where $[P_h]$ in Eq. (12) denotes the jump in the pressure across the edges of an element, k, and $\{P_h\}$ denotes the average of pressure across the edge, $\partial\Omega_k$. s_k is evaluated for all the edges of an element, Ω_k in the domain. Following criteria (Eq. (13)) is used to identify the regions of the shock from the smooth flow regions. Shock locations are identified for s_k greater than a threshold value of 0.3 (this gives optimum performance) and smooth flow regions are identified for $s_k \leq 0.3$

$$\begin{cases} s_k > 0.3; p = 0, \text{shock\_region} \\ s_k \leq 0.3; p \geq 1, \text{smooth\_region}. \end{cases} \tag{13}$$

A switch "lim" is used to identify shock regions and an example is shown in Fig. 4 for hypersonic flow around a cylinder. $p = 0$ is the red region indicating shock and $p \geq 1$ is used in the blue region, indicating smooth flow regions. Solution accuracy in smooth flow regions can be improved by increasing the order of polynomial approximation, p, without changing the mesh resolution there. This is the advantage afforded by DG method. But, the shock region is limited to $p = 0$ and hence first order accurate. A reasonable way to improve solution accuracy in the shock region is to refine the mesh. One approach taken in Refs. 54 and 55 is applying h-refinement in the shock regions. This improves the solution accuracy in the shock regions. However, this also results in large number of elements in the region around the shock, which may not lie in the shock. For this purpose, we use the r-adaptivity approach, where we cluster the elements in the domain outside of the shock, to a region very close to the shock. This refinement is based on the shock location, and hence applicable to all body shapes. Successive r-p adaptivity iterations resulting in increasingly finer mesh resolution at the shock are shown in Fig. 4(b)–4(d). We have also implemented parallelization of MIG using two parallel solver platforms, HYPRE[59] and PETSc.[60] These simulations are run using PETSc parallel solver.

V. PROBLEM DESCRIPTION

In this work, we consider the effect of plasma DBD actuators on a Mach 17 hypersonic flow over a cylinder, of radius 1 m, both with and without thermo-chemistry (presented in Secs. VI and VII, respectively). Air is considered as a perfect gas for viscous hypersonic flow, and a mixture of N_2 and O_2 for non-equilibrium hypersonic flow. For both simulations, with and without thermo-chemistry, a free-stream temperature of 200 K and a fixed cylinder wall temperature of 500 K is assumed. The free-stream and boundary conditions are summarized in Table I, for flows with and without thermo-chemistry.

For the non-equilibrium flow, the mass fractions of N_2 and O_2 are in a ratio of 0.7562:0.2438 in the free-stream. Air is also considered to be in thermo-chemical equilibrium in the free-stream, hence the vibrational temperature for air is equal to its translational-rotational temperature, i.e., $T_v = 200$ K. Super-catalytic wall forces the flow species, near the wall, into thermo-chemical equilibrium. Hence, the vibrational temperature at the wall is equal to the fixed wall

TABLE I. Free stream and boundary conditions for M17 hypersonic flow over cylinder.

Free stream and boundary conditions	Without thermo-chemistry	With thermo-chemistry
Mach number, M_∞	17.65	17.65
Density, ρ_∞ (kg/m3)	0.001	0.001
x-velocity, u_∞ (m/s)	5000	5000
T_∞ (K)	200	200
T_{wall} (K)	500 (fixed temperature wall)	500 (fixed temperature and super catalytic wall)
u, v (@wall) (m/s)	0 (no slip wall)	0 (no slip wall)

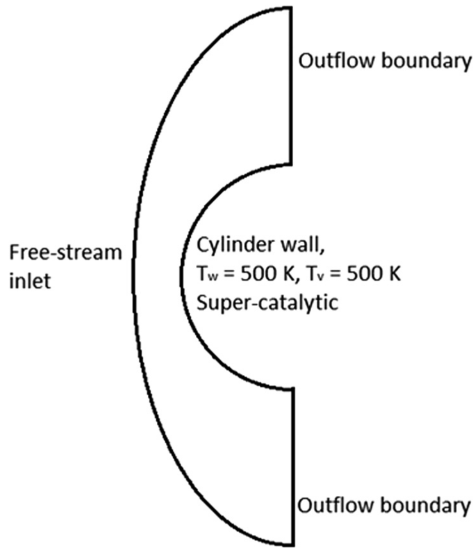

FIG. 5. Boundary conditions summarized for the four edges of the domain. Free-stream inlet is at the left of the domain and the cylinder wall at the right. Outflow boundary conditions are used on the two edges on top and bottom of cylinder.

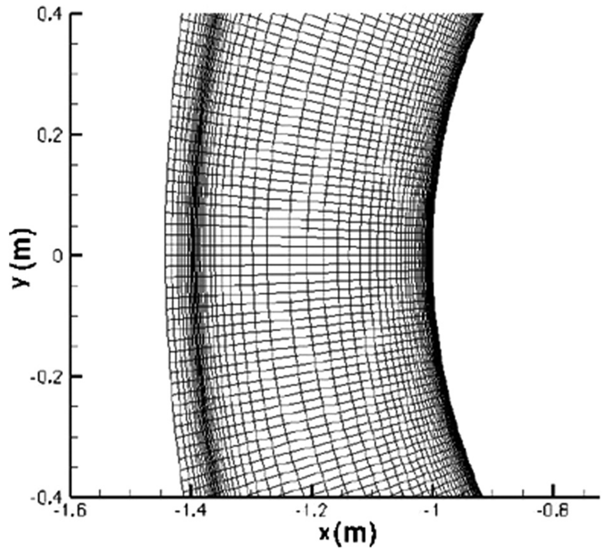

FIG. 6. Mesh used for plasma actuation of viscous hypersonic flow has 256×100 elements. This is achieved after 4th r-p adaptivity iteration. This mesh shows very fine mesh obtained at the shock.

temperature of 500 K, and all the species recombine at the wall to give free-stream species at the wall.

The boundary conditions are shown in Fig. 5. The out flow is set to be supersonic, but the boundary layer is not. Having incorrect boundary layer profile for the outflow, however, will not affect results near the stagnation region.

VI. EFFECT OF PLASMA DBD ACTUATORS ON VISCOUS HYPERSONIC FLOWS

First, we look into the effect of micro-second pulsed DBD plasma actuators on a viscous perfect gas hypersonic flow. The body force, as a result of plasma actuation, is first applied at the stagnation point on the cylinder surface. We first note the effect of this actuation, on the heat transfer coefficient, C_h, in order to enhance our understanding of the physics of this problem. Various designs for plasma actuators are then considered, by varying locations and polarity (i.e., direction of the force) of the plasma actuation. This grid has 256×100 elements in the domain, where the 256 elements are uniformly distributed in the θ (or circumferential) direction and 100 elements, with varying sizes, are distributed along the radial direction. A part of final r-p adapted grid is shown in Fig. 6.

We consider three configurations, as shown in Fig. 7, for the placement of plasma DBD actuators on the cylinder. "Plasma1" refers to the first configuration with the plasma actuator placed at the stagnation point, with body force in the +y-direction. For the second and third configurations, two plasma actuators are placed symmetrically on the cylinder surface, at a distance of 25 mm (measured along the circumference of the cylinder) away from the stagnation point in the positive and negative y-directions. In the second configuration or "plasma2," both plasma actuators apply body force away from each other, i.e., plasma actuator in the positive part of y-axis, applies force in the +y-direction and the plasma actuator, in the negative part of y-axis, applies force in -y-direction. In the third configuration, i.e., "plasma3," the directions of both forces are reversed (from "plasma2"), so that both the forces act towards each other. The schematic in Fig. 7 illustrates the three configurations. The effect of these three configurations on the C_h profile is summarized in Fig. 8.

C_h measures the ratio of heat transferred to the solid surface (from the fluid) to the thermal capacity of the fluid. Its formula is given in

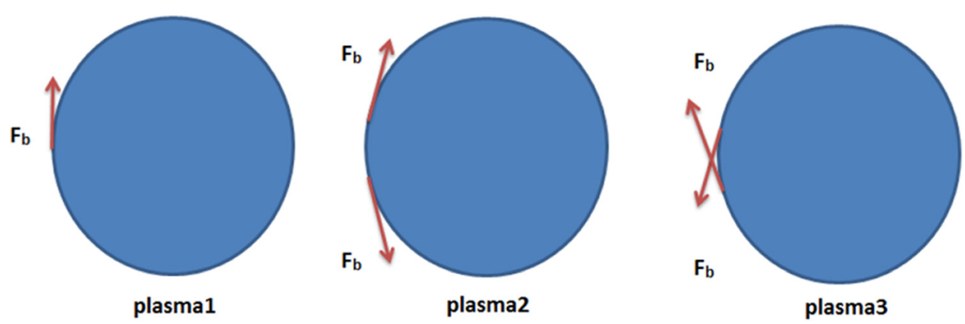

FIG. 7. Three configurations for plasma DBD actuators. In the first configuration, plasma actuator is applied at the stagnation point, with flow forcing in the positive y-direction. Second and third configurations have same placements of the actuators, i.e., ±25 mm distance from the stagnation point along the circumference of the cylinder, but with reversed flow forcing. Second configuration has forces pointing away from each other and third configuration has forces pointing towards each other.

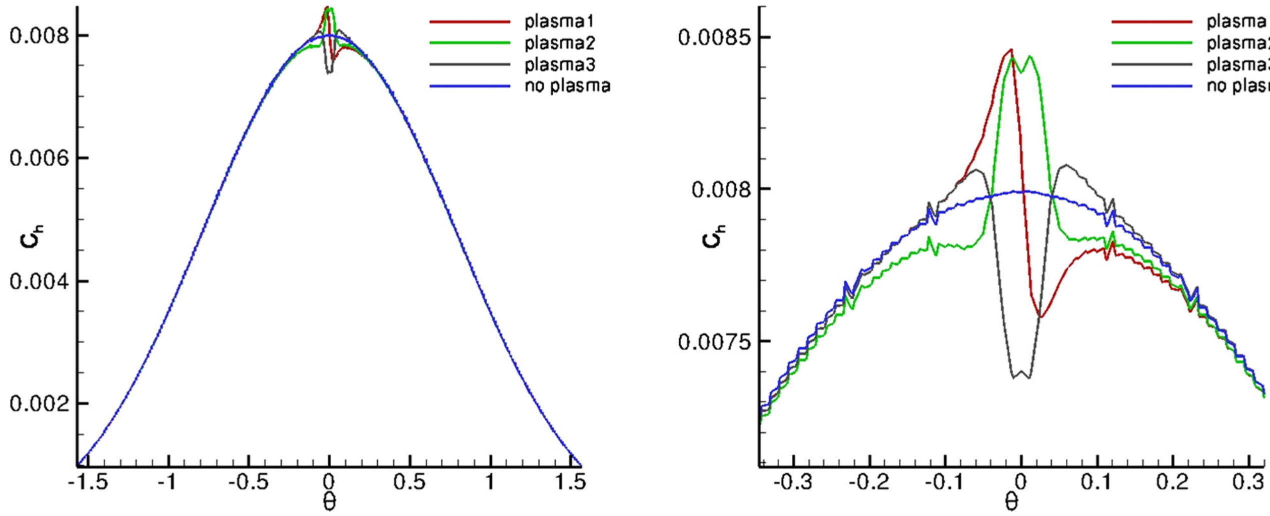

FIG. 8. Effect of plasma actuation on the surface heat transfer coefficient, C_h of hypersonic flow over cylinder problem shown in (a) zoomed in section and in (b) full plot. The case of "no plasma" from MIG, compares well to C_h profile predicted from LAURA.[62] The comparisons of C_h profile for "plasma1," "plasma2," and "plasma3" are also shown. Best reduction of C_h profile is obtained for plasma3.

$$C_h = \frac{q_w}{\frac{1}{2}\rho_\infty U_\infty^3}, \tag{14}$$

where $(q)_w$ is the net heat flux in the wall normal direction.

The plasma1 configuration leads to both an increase and reduction of C_h profile along the surface of the cylinder. A maximum value of 0.00846, occurs at $\theta = -0.0136$ (very close to stagnation point), and minimum value of 0.00758 occurs at $\theta = 0.025$. Since the radius is 1 m, these locations correspond to -13.6 mm and 25 mm distance away from stagnation point (along the cylinder circumference). Upon performing integration over the entire surface, we can see that the plasma actuator in the "plasma1" configuration provides net cooling effect. The other two configurations, plasma2 and plasma3 are similar to moving the plasma DBD effect on C_h profile (in plasma1) in ± 25 mm direction to the location of plasma actuator, and reversing the C_h profile based on the direction of the plasma body force. Thus, the second and third configurations give overall heat transfer increment and reduction, respectively.

To understand the flow physics, the effect of the plasma actuator on the temperature and velocity profiles, near the wall (in direction normal to the wall), is analyzed, w.r.t. "no plasma" case. For "plasma1" configuration, the effect of the actuator is shown in Fig. 9, both with and without plasma. Visually, the temperature contours are pushed closer to the cylinder surface for negative y-axis and away from the surface for positive y-axis, for "plasma1" relative to "no plasma" case. Thus, the actuator reduces the C_h value at about 25 mm distance downstream from its actual location, by strongly pushing the temperature contours away from the cylinder surface.

It can therefore be seen that the micro-second pulsed plasma DBD actuator, which are generally considered only appropriate for subsonic flows, have significant effect on hypersonic flows (near the boundary layer), in terms of heating. This is due to the large stagnation region in the hypersonic flow, with low velocities next to the wall that allows

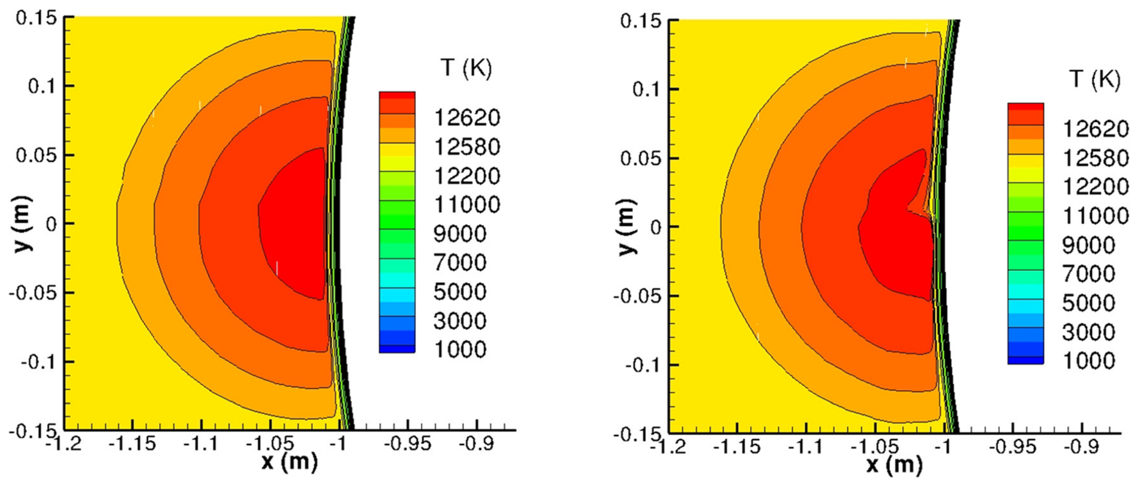

FIG. 9. Effect of "no plasma" vs plasma actuator in "plasma1" configuration on the temperature contours close to the stagnation region of the cylinder.

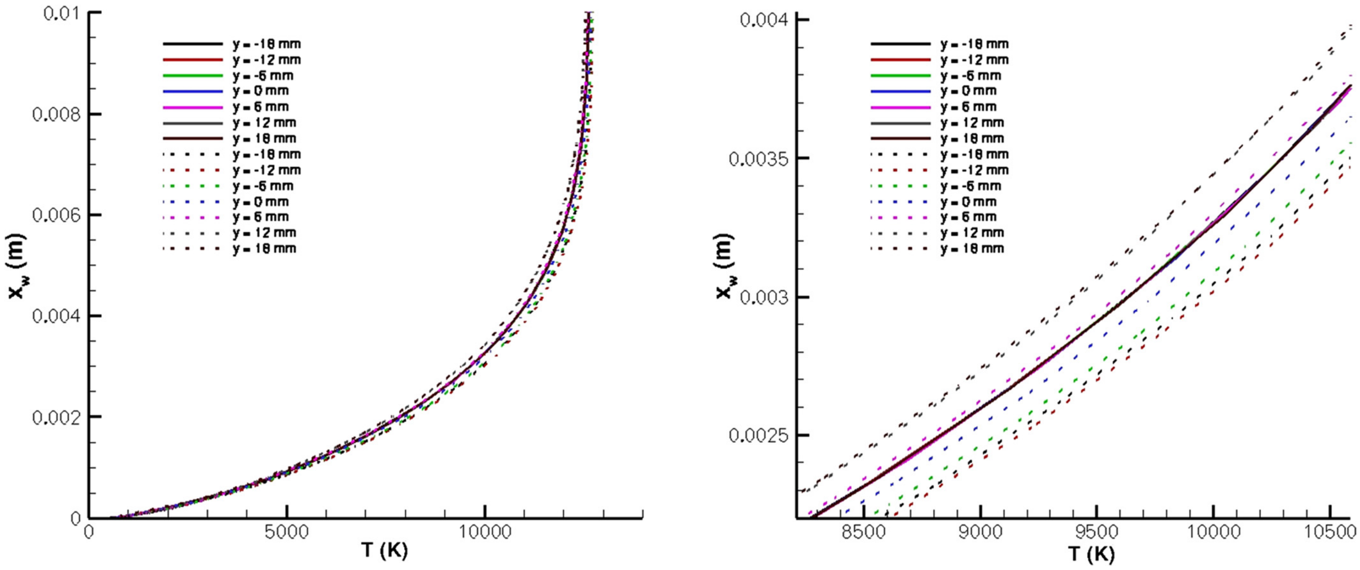

FIG. 10. Temperature plots in the flow, shown with distance (in the flow) away from the wall, denoted as x_w. (a) Overall plot for different y-locations (shown in the legend) and (b) zoomed-in section. Y-locations correspond to the distances traveled along the cylinder surface in the positive or negative direction from the stagnation point. Solid lines refer to the results without plasma and dotted lines refer to the results with plasma (plasma1).

the plasma actuator to make some significant effect on the surface heating in hypersonic flow, by adding momentum into the flow.

Next, we look at the temperature and velocity profiles (Figs. 10 and 11), near the cylinder surface, as we move away from the wall in the normal direction. We notice from Fig. 10 that all the temperature profiles fall into a single curve for the "no plasma" case. For "plasma1" case, the temperature profiles are above and below relative to the profiles of the "no plasma" case for locations closer to the actuation point and in the positive and negative half of y-axis, respectively. This corresponds to the increment and decrement observed in C_h profile in Fig. 8. From Fig. 10, we note that the maximum value of C_h is at -12.5 mm, close to -13.6 mm, seen in Fig. 8. Velocity profiles in Fig. 11 indicate significant increase in y-velocity, from 1 m/s to 8.5 m/s, at a distance of nearly 1 mm away from cylinder surface at the stagnation point.

The temperature contours for second and third configuration (close to the stagnation region) are shown in Fig. 12. In "plasma2" configuration, the temperature contours are compressed closer to the surface, relative to "no plasma" case, from $y = -50$ mm to $+50$ mm. Thus, C_h value for plasma2 configuration is higher than "no plasma" case for $\theta = -0.05$–0.05. For the rest of the region, C_h profile falls below the C_h profile for the "no plasma" case.

Correspondingly for "plasma3" configuration, the temperature contours are pushed away from the cylinder wall,

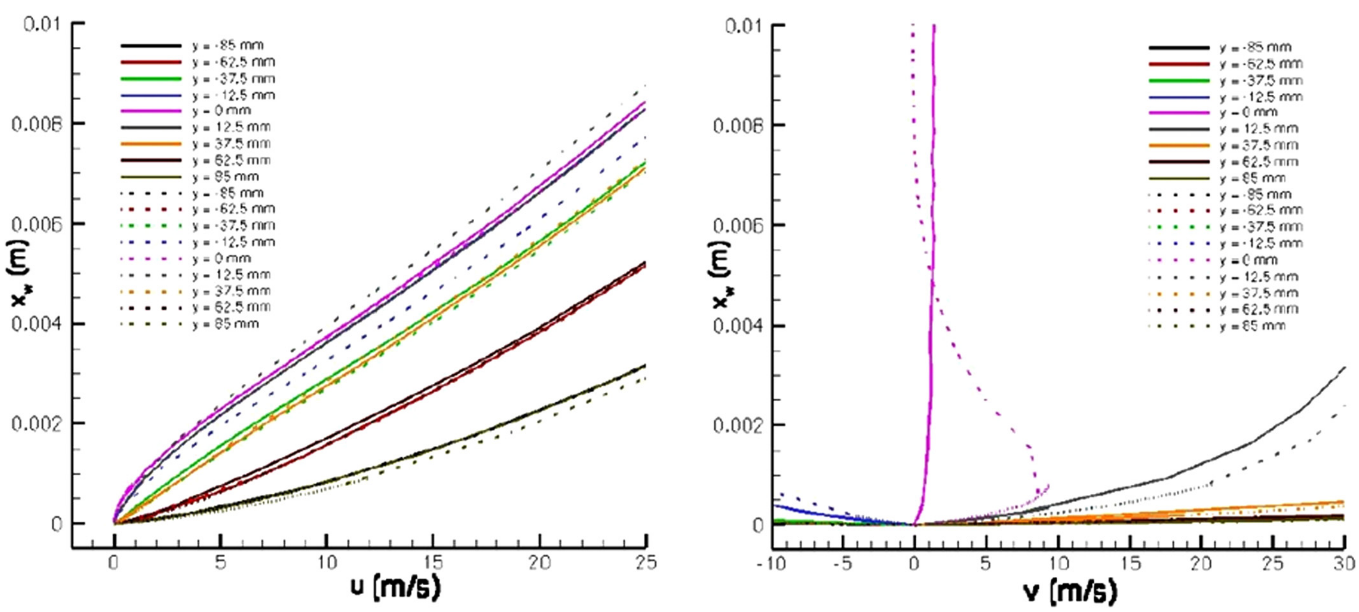

FIG. 11. X and Y velocity profiles shown with x_w, the distance measured in the wall normal direction, away from the wall. Y-velocity is almost parallel to the cylinder surface, near the stagnation point, and is thus relevant to understand the cause of observed change in C_h value near stagnation point.

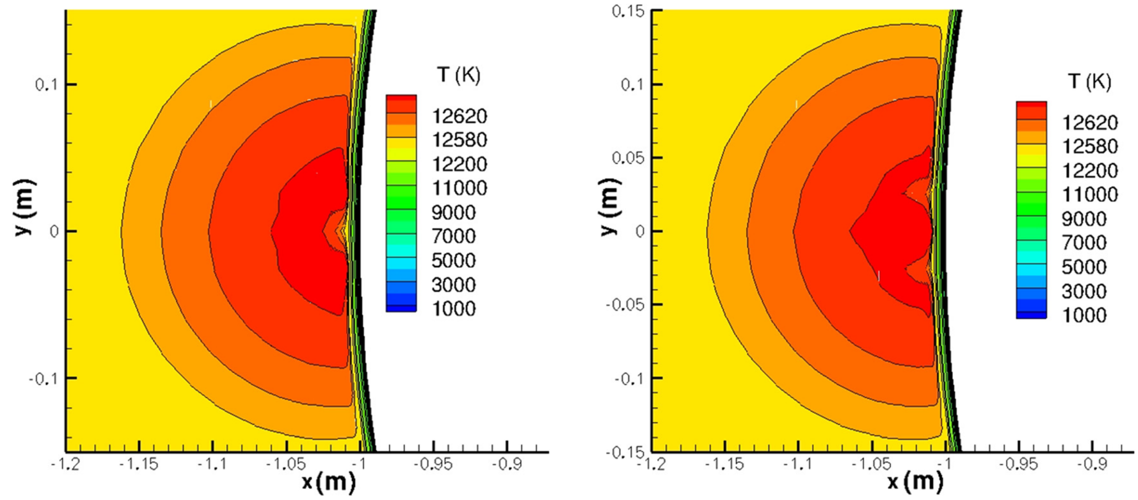

FIG. 12. Temperature contours near stagnation region for two plasma actuators at 25 mm (w.r.t. stagnation point on cylinder surface), acting (a) with body forces pointed away from each other, i.e., plasma2 configuration and (b) with body forces pointed towards each other, i.e., plasma3 configuration.

for y = −50 mm to +50 mm, thus causing overall reduction in C_h value relative to "no plasma" case. What causes the temperature contours to be pulled into or pushed away from the wall in plasma2 and plasma3 configurations is explained through the velocity schematic given in Fig. 13, for "plasma1" configuration. Plasma body force induces a flow (shown in red) in the direction of the force. The oncoming flow (shown in blue) hits the cylinder surface (approximated by a flat wall in black). Without the plasma body force, the flow has zero tangential velocity (y-velocity) a few millimeter distance away from the wall, and hence maximum value of C_h is experienced at the stagnation region. The flow induced, by the plasma, causes a leftward shift (from the stagnation point) of the point of zero tangential velocity. This causes the maximum in C_h to shift slightly to the left in Fig. 8. The question, that arises, is why C_h profile shoots above the maximum value of C_h at the stagnation point for "no plasma" case.

Velocity profiles, induced by the plasma actuator in the "plasma1" configuration, relative to "no plasma" case are shown in Fig. 14. Actuator decelerates the flow (going in the negative direction), to the left of the stagnation point, hence causing increased heating at the surface there, and accelerates the flow, to the right of the stagnation point, hence reducing heat transfer to that surface. Suction of the high temperature gas causes increased heat transfer, below the stagnation point. Added momentum pushes away the high temperature gas (from the wall), resulting in reduced heat transfer, above the stagnation point. Temperature profiles for plasma2 and plasma3 configurations in comparison to "no plasma" case are given in Fig. 15. It can be seen above that temperature profiles for the "plasma2" case, primarily lie below the temperature profile for "no plasma" case and that for "plasma3" case, primarily lie above the "no plasma" case, thus being consistent with higher and lower C_h profiles observed for "plasma2" and "plasma3" cases, respectively, in reference to "no plasma" case.

Same observation is also made in the y-velocity profiles for "plasma2" and "plasma3" cases (see Fig. 16). Here, the plasma DBD actuator located in the positive y-axis,

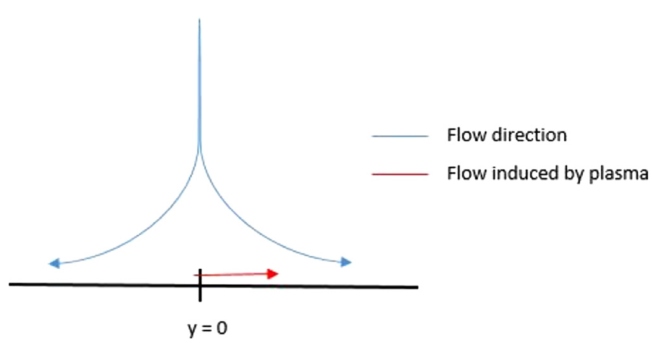

FIG. 13. Schematic of flow induced (in red) by plasma body force with force direction in +y direction. The oncoming flow (in blue) hits the wall (in black). The cylinder surface close to the stagnation region can be approximated by a flat wall.

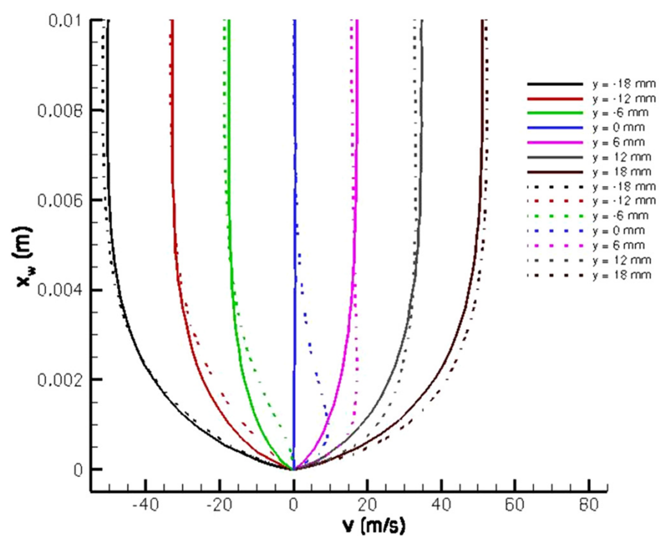

FIG. 14. Y-velocity, v (m/s) (parallel to the cylinder wall) is generated for several locations close to the stagnation point, lying both to the left and the right. This is plotted for both with and without plasma actuators (solid lines represents the case without plasma actuator and dotted lines, the case with the plasma actuator). This plot is for comparison of "plasma1" case to "no plasma" case.

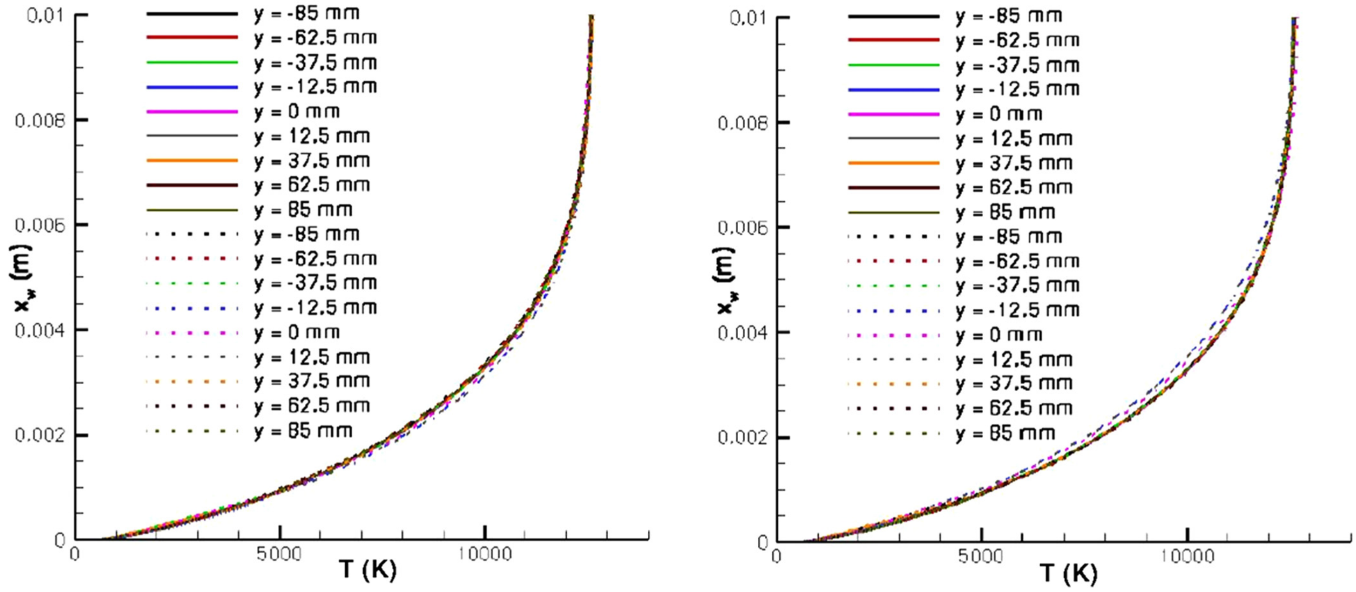

FIG. 15. Temperature profiles for "plasma2" and "plasma3" configurations in comparison to the "no plasma" case. For plasma2 case, the temperature profiles (shown in dotted profile) have steeper gradient than "no plasma" case and for "plasma3" case, the temperature gradient has lower gradient.

introduces a wall jet in the direction of the fluid flow in the "plasma2" configuration and in the opposite direction of the fluid flow in the "plasma3" configuration. By increasing the flow velocity next to the wall, the plasma actuator is able to entrain more of the high temperature fluid, thus producing more surface heating for "plasma2" configuration, and by decreasing the flow velocity next to the wall, it is able to push the high temperature fluid away from the wall, thus reducing heating next to the wall for plasma3 configuration.

VII. EFFECT OF PLASMA DBD ACTUATORS ON NON-EQUILIBRIUM HYPERSONIC FLOWS

After successfully looking into the effect of plasma DBD actuator on the Mach 17 flow over hypersonic flow, we investigate its effect on a cylinder in hypersonic flow with thermo-chemical non-equilibrium. But before this, we show basic comparison of results for MIG with the US3D code developed at the University of Minnesota.[61] US3D is an unstructured CFD code for hypersonic flow solution used extensively to solve many different hypersonic flow problems and has gone through extensive validation and verification. The mesh used in MIG, for thermo-chemical non-equilibrium hypersonic flow simulation, is shown in Fig. 17. This was obtained after the 4th r-p adaptivity iteration.

Temperature contours for $N_2 + O_2$ case are shown in Fig. 17 for both MIG and US3D. Both the results compare very well to each other. The maximum temperature in MIG is found to be 7700 K and in US3D to be 6500 K. This difference results from finer mesh used in MIG, from the successive (4th) r-p adaptivity iteration, in comparison to coarser mesh being used in US3D. The temperature contours show a

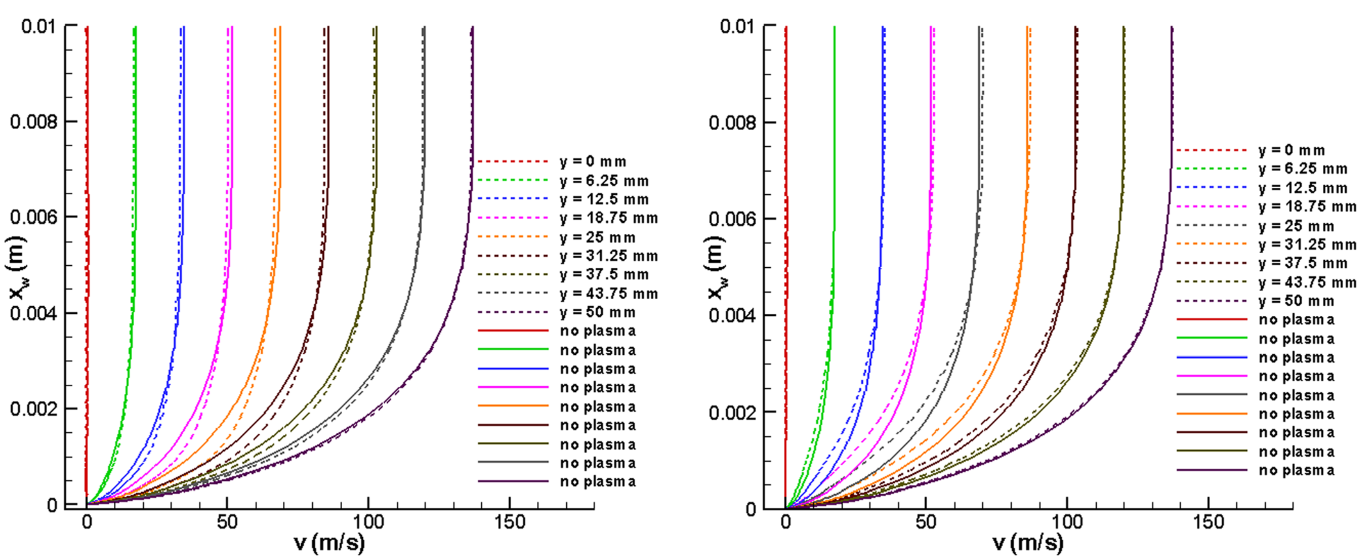

FIG. 16. Y-velocity profiles for "plasma2" and "plasma3" configurations in comparison to "no plasma" case. In plasma2 configuration, flow is accelerated, and in plasma3 configuration, flow is decelerated relative to "no plasma" case.

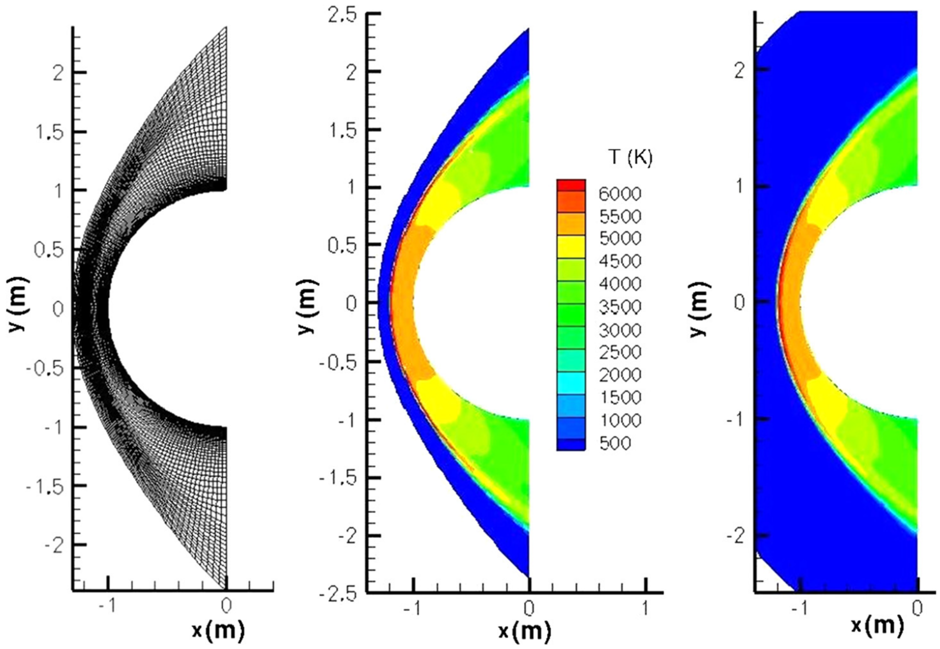

FIG. 17. Mesh and comparisons of temperature contours for Mach 17 non-equilibrium hypersonic flow. (a) Mesh obtained after 4th r-p adaptivity iteration for MIG, (b) temperature contours comparison obtained from MIG code, and (c) US3D code. Both results compare very well to each other. Maximum temperature in MIG is 7700 K and in US3D is 6500 K, and the difference is due to finer mesh at the shock in MIG obtained with successive (4th) r-p-adaptivity iteration in comparison to coarser mesh at the shock for US3D.

spiked nature in the shock and a smoothed out nature to the inside of the shock layer. This results from strong thermo-chemical non-equilibrium within the shock, which quickly equilibrates in the shock layer, due to large number of molecular collisions.

Contours for vibrational temperature also compare very well for MIG and US3D (see Fig. 18). For T_v, the maximum temperature in flow field for MIG is 6300 K and for US3D is 6550 K. Hence, the maximum values of vibrational temperature are much closer for both the codes than it is for the maximum values of translational-rotational temperature. Contours for mass fraction of O_2 are shown in Fig. 18, and both codes show complete dissociation of O_2 in the shock layer. This is due to temperatures exceeding 2000 K. Corresponding results for mass fractions of O are seen in Fig. 19. Dissociation of N_2 into N atoms is incomplete with maximum dissociation (of nearly 0.07 of total mass fraction, see Fig. 19) occurring just after the shock. Significant dissociation of N_2 requires higher temperatures, of the order of 7000 K or higher. A small portion of the atomic nitrogen, N (produced by the dissociation), combines with atomic oxygen, O to form NO close to the shock region (Fig. 20). Away from the shock, in the shock

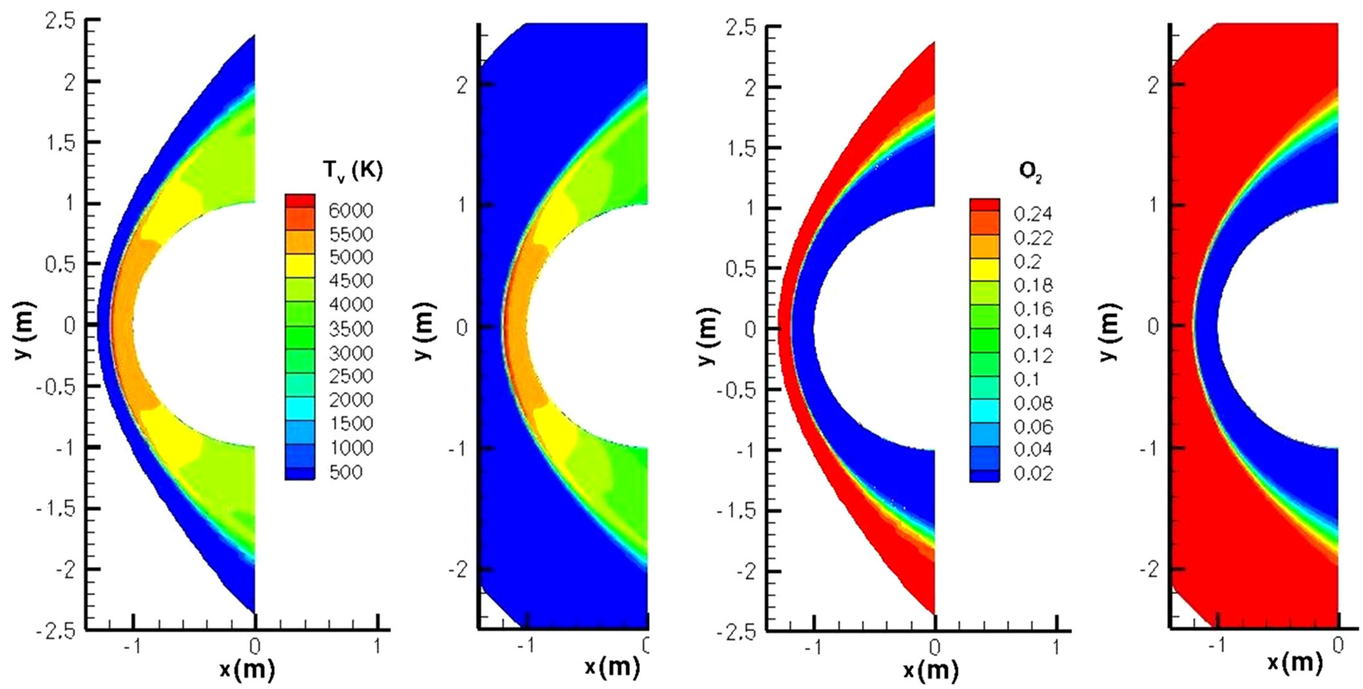

FIG. 18. Contours for vibrational temperature for (a) MIG and (b) US3D, and mass fraction of O_2 for (c) MIG and (d) US3D. Both results compare very well to each other. Maximum vibrational temperature in MIG is 6300 K and in US3D is 6550 K, and the difference is again attributed to meshing difference in both the codes. For O_2, a complete dissociation is noticed in both the codes.

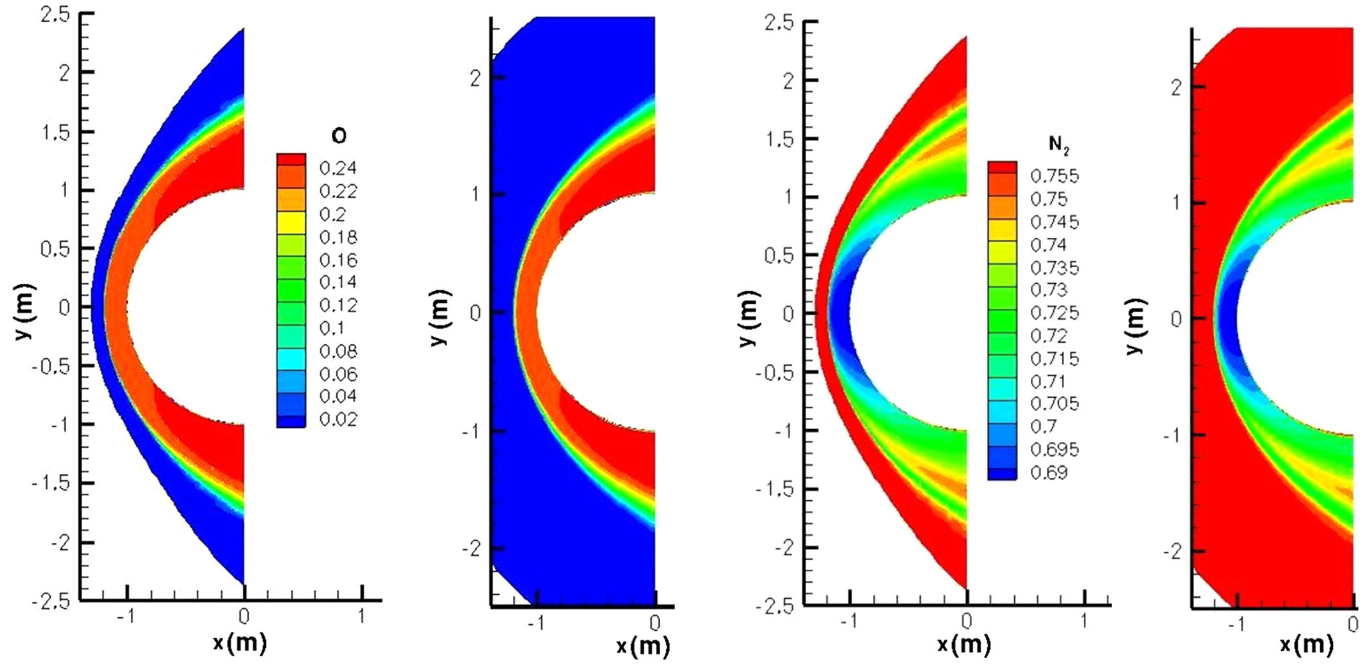

FIG. 19. Mass contours of O for (a) MIG, (b) US3D and N_2 for (c) MIG and (d) US3D. Comparisons are fairly accurate. Maximum mass fraction for O, i.e., 0.2438, is found close to the top and bottom regions of the cylinder. This correlates to the mass fraction of NO, in that the maximum O is observed, when NO (formed in the shock) dissociates into N and O (due to lower temperature in the shock layer) giving extra O. A partial dissociation of N_2 is observed close to the stagnation region, as the temperature is not of order of 7000 K or higher for significant dissociation.

layer, the temperatures are not high enough to sustain NO which again dissociates into atomic N and O. Thus, in the contours of N, we see the maximum value of mass fraction being just after the shock rather than in the shock.

As N_2 and O_2 continue to dissociate past the shock, the temperature contours which have a maximum in the shock, continue to drop unlike purely viscous case, where the temperature increases as the flow stagnates until the viscous boundary layer is reached. As we go away from the stagnation line towards either the top or bottom of cylinder, the temperature values decrease, and hence the amount of NO (dissociating into N and O) also decreases, thus we see that maximum mass fraction of O is at top and bottom regions of cylinder and not near the stagnation line.

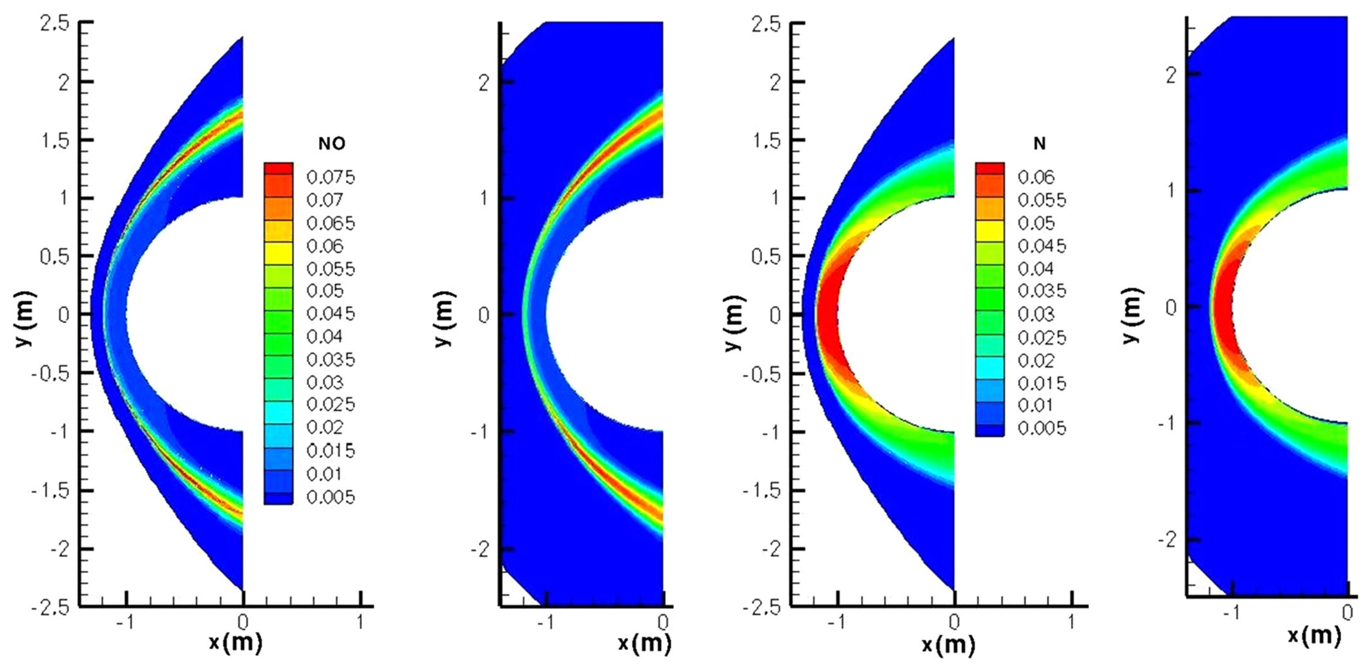

FIG. 20. Mass fraction contours of NO for (a) MIG and (b) US3D and of N for (c) MIG and (d) US3D. Maximum mass fraction for NO and its production occurs in the shock by combination of atomic N and O produced by dissociation reactions of N_2 and O_2 molecules. As the temperatures, being maximum at the shock, drop down in the shock layer, NO again dissociates back into N and O atoms. Production of atomic N corresponds to the dissociation of N_2 shown in Fig. 19.

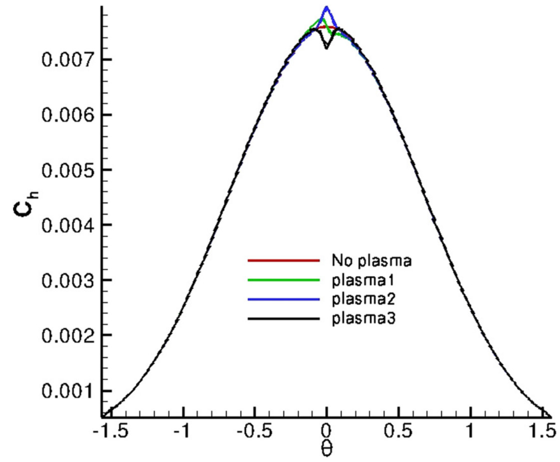

FIG. 21. The effect of the plasma DBD actuator on C_h profile, for non-equilibrium hypersonic flow is shown. In reference to the base case, with no plasma (shown in red), plasma1 case gives both increase and decrease in C_h value, plasma2 case gives overall increase in C_h value and plasma3, as expected, gives overall reduction of heating.

Having verified our non-equilibrium hypersonic flow code with US3D, we now investigate the effect of the plasma actuators (in three configurations shown in Fig. 7) on the non-equilibrium hypersonic flow. Just as in Sec. VI, we look at the effect on the surface heating profile (Fig. 21). The effect is similar to Fig. 8, which is expected. In non-equilibrium hypersonic flow, the heat flux into the wall is equal to net conduction based on both translational-rotational and vibrational temperatures, i.e., T and T_v, and the enthalpy transport of diffusing species close to the wall. Comparing plasma3 configuration to the base case of no plasma, reduction of temperature gradient (at stagnation line) next to the wall is observed (Fig. 22). This is true for both translational-rotational temperature, T, and vibrational temperature, T_v. The effect is dominant to within 10 mm distance away from the wall. In addition to the temperature profiles, the application of plasma DBD actuator is also seen to have effect on the species mass fractions. This effect is not so pronounced for O_2 and O, as can be seen in Fig. 23.

However, a more significant effect is seen on stagnation line plots for N and NO (in Fig. 24). The difference of plasma3 case, w.r.t. the base case is seen up to 25 mm distance away from the wall. In Fig. 24(a), we notice sudden reduction of N, close to the wall, for both with and without the plasma actuator. This happens from a reduction in temperature, close to the wall (due to the boundary condition). At lower temperatures, nitrogen cannot sustain in the atomic form, and hence recombines to N_2 (primarily) and NO near the wall. This recombination releases large amount of heating to the wall. A minor change in temperature, because of plasma, causes significant variation in mass fraction of N, up to distance of 25 mm away from wall. For NO, there is increase in mass fraction, close to the wall (from 4 mm to 2 mm next to the wall). This is due to atomic N and O

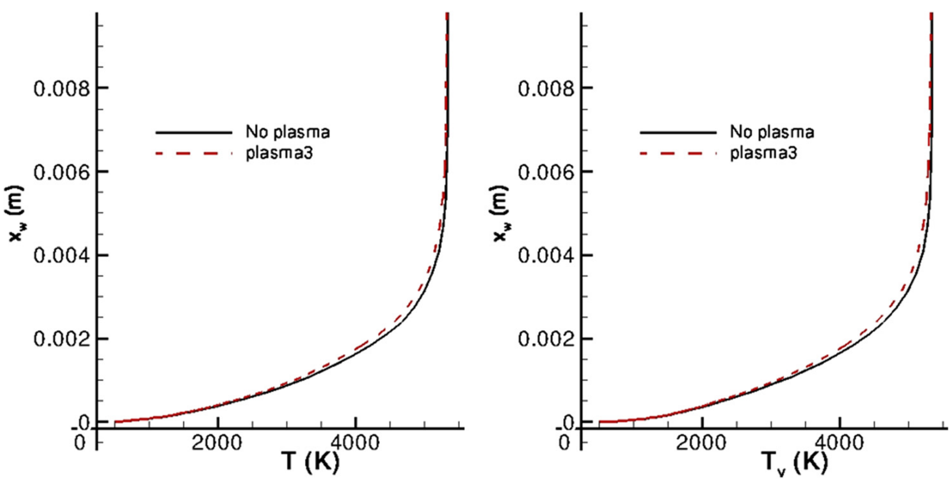

FIG. 22. Effect of plasma3 configuration on stagnation line plots of T and T_v is shown next to the wall, in reference to "no plasma" case. Only a minor effect is seen in the temperature plots for distance up to 10 mm away from cylinder wall.

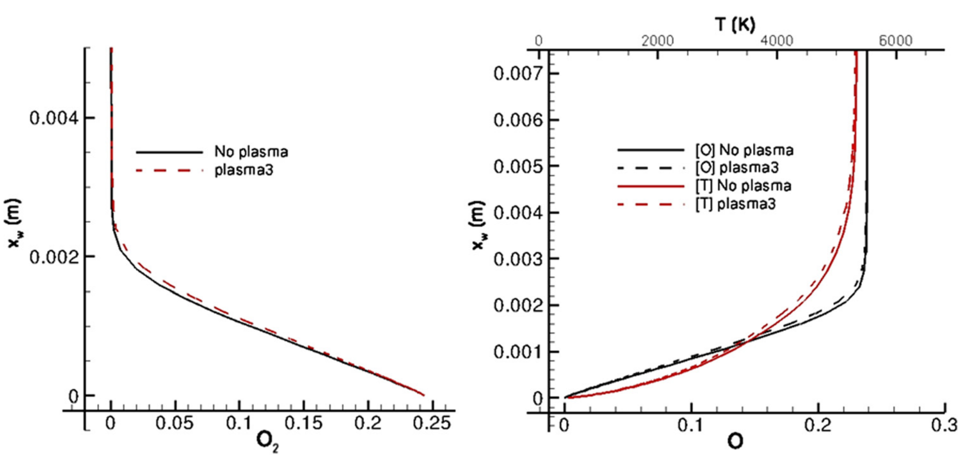

FIG. 23. Effect of plasma3 configuration on stagnation line plots of O_2 and O, is shown next to the wall, in reference to "no plasma" case. Only a minor effect is seen in the plots for distance up to 6 mm away from cylinder wall.

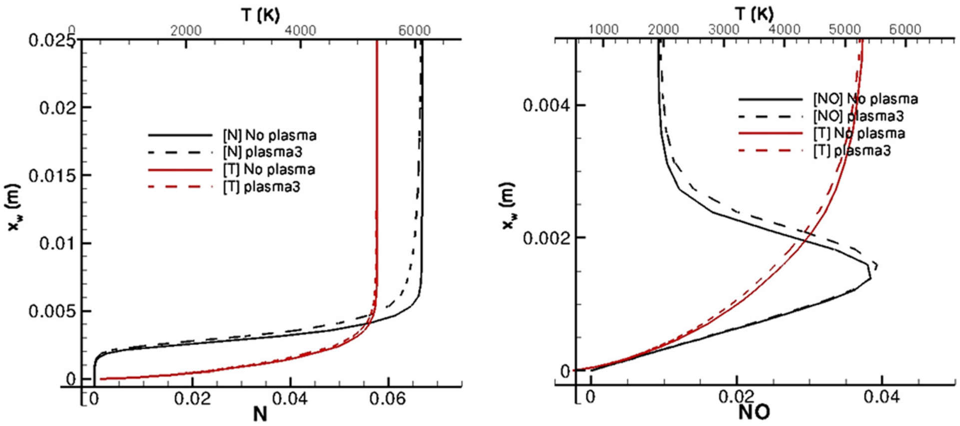

FIG. 24. Effect of plasma3 configuration on stagnation line plots of N and NO, is shown next to the wall, in reference to "no plasma" case. Significant difference is noted in the mass fractions of N and NO, due to plasma DBD actuator in plasma3 configuration. For N, the effect is seen up till 25 mm distance away from wall.

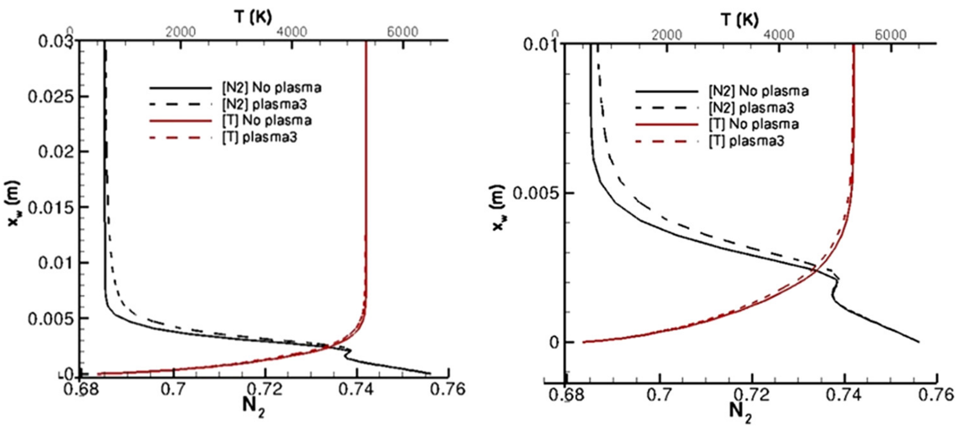

FIG. 25. Effect of plasma actuator on N_2 near the wall. (a) Effect of plasma3 configuration on stagnation line plot of N_2 near the wall, and its (b) zoom-in section. A significant difference is seen in curves for N_2 up to 30 mm distance away from wall.

recombining into N_2, O_2, and NO. For the distance of 2 mm away from the wall, even NO species vanishes due to the super-catalytic wall boundary condition. Hence, a small peak for NO is observed in Fig. 24(b).

Plot of N_2, in Fig. 25, shows that its mass fraction increases in two phases when approaching wall. From 30 mm to 2 mm distance from the wall, N_2 monotonically increases, after which there is a dip in its mass fraction. This is due to mass fraction of NO increasing at a distance of 2 mm close to wall. When NO start decreasing at approximately 1.5 mm distance away from wall, N_2 again begins to increase in its mass fraction. Thus, significant effect of plasma DBD actuators is noted on hypersonic flows, both with and without thermo-chemistry.

VIII. CONCLUSION

We simulated Mach 17 hypersonic flow over a cylinder, with and without thermo-chemistry, using discontinuous Galerkin method. The effect of micro-second pulsed, sinusoidal DBD plasma actuators on the hypersonic flow was investigated with three actuator configurations. A significant change in the surface heat transfer was predicted. A specific configuration with opposing plasma injected momenta resulted in maximum reduction of 7.68% in the stagnation point heat flux. Low magnitude of flow velocity near the stagnation point makes actuation effective. The wall jet induced by the plasma actuator influences the temperature contours near the actuator location. This pull and push mechanism is responsible for the increment and decrement of existing local heat flux upstream and downstream of plasma actuator, respectively.

In the two different configurations with a pair of plasma actuators placed at a distance of 50 mm (away from each other) on the cylinder surface, the second configuration gives overall reduction in the surface heating coefficient. Thus, we demonstrate, that the micro-second plasma DBD actuators, though conventionally thought of as being ineffective for high speed flows, do have significant effect on the surface heating distribution of the cylinder.

In addition, the effect of thermo-chemistry on the plasma actuation of hypersonic flow was also studied, using 5 species finite rate air chemistry with 17 reactions. In addition to affecting temperature profiles next to the wall, plasma actuators also affect the species concentration distribution near the wall. The effect is significant for N_2, N, and NO. Based on the effect on temperature gradient and species concentration, a maximum reduction of 4.04% in the stagnation point heat flux was predicted for this case. This shows promise for the use of the plasma DBD actuators for the integrated surface heating reduction in hypersonic flows.

ACKNOWLEDGMENTS

The authors gratefully acknowledge the partial support provided by Air Force Research Laboratory and Mechanical & Aerospace Engineering Department at University of Florida, for this work. This journal paper has been cleared for Public Release, with Case No. 88ABW-2014-2808.

[1]J. R. Roth, D. M. Sherman, and S. P. Wilkinson, "Electrohydrodynamic flow control with a glow discharge," AIAA J. **38**, 1166–1172 (2000).
[2]F. Soetomo, "The influence of high voltage discharge on flat plate drag at low Reynolds number air flow," MS thesis (Iowa State University, 1992).
[3]J. R. Roth, D. M. Sherman, and S. P. Wilkinson, "Boundary layer flow control with a one atmosphere uniform glow discharge surface plasma," AIAA Paper 98-0328, 1998.
[4]L. Leger, E. Moreau, G. Artana, and G. Touchard, "Influence of a DC corona discharge on the airflow along an inclined flat plate," J. Electrostat. **51–52**, 300–306 (2001).
[5]L. Leger, E. Moreau, and G. Touchard, "Control of low velocity airflow along a flat plate with a DC electrical discharge," in Proceedings of IEEE-IAS World Conference on Industrial Applications of Electrical Energy, Chicago, USA, 2001.
[6]E. Moreau, L. Leger, and G. Touchard, "Effect of a DC surface non-thermal plasma on a flat plate boundary layer for airflow velocity up to 25 ms−1," J. Electrostat. **64**, 215–225 (2006).
[7]M. Riherd and S. Roy, "Serpentine geometry plasma actuators for flow control," J. Appl. Phys. **114**(8), 083303 (2013).
[8]M. Samimy, I. Adamovich, B. Webb, J. Kastner, J. Hileman, S. Keshav, and P. Palm, "Development and characterization of plasma actuators for high speed and reynolds number jet control," Exp. Fluids **37**(4), 577–588 (2004).
[9]M. Samimy, I. Adamovich, J.-H. Kim, B. Webb, S. Keshav, and Y. Utkin, "Active control of high speed jets using localized arc filament plasma actuators," AIAA Paper 2130, 2004.
[10]N. Bisek, J. Poggie, M. Nishihara, and I. Adamovich, "Computational and experimental analysis of Mach 5 air flow over a cylinder with a nanosecond pulse discharge," AIAA Paper 2012-186, 2012.
[11]J.-H. Kim, M. Nishihara, I. V. Adamovich, M. Samimy, S. V. Gorbatov, and F. V. Pliavaka, "Development of localized arc filament RF plasma actuators for high-speed and high Reynolds number flow control," Exp. fluids **49**(2), 497–511 (2010).
[12]P. Bletzinger, B. N. Ganguly, W. D. Van, and A. Garscadden, "Plasmas in high speed aerodynamics," J. Phys. D: Appl. Phys. **38**, R33–R57 (2005).
[13]V. E. Semenov, V. G. Bondarenko, V. B. Gildenburg, V. M. Gubchenko, and A. I. Smirnov, "Weakly ionized plasmas in aerospace applications," Plasma Phys. Controlled Fusion **44**, B293–B305 (2002).
[14]J. S. Shang, "Plasma injection for hypersonic blunt-body drag reduction," AIAA J. **40**(6), 1178–1186 (2002).
[15]J. S. Shang, S. T. Surzhikov, R. Kimmel, D. Gaitonde, J. Menart, and J. Hayes, "Mechanisms of plasma actuators for hypersonic flow control," Prog. Aerosp. Sci. **41**(8), 642–668 (2005).
[16]C. Park, U. B. Mehta, and D. W. Bogdanoff, "MHD energy bypass scramjet performance with real gas effects," J. Propul. Power **17**(5), 1049–1057 (2001).
[17]D. Gaitonde, "Three-dimensional flow-through scramjet simulation with MGD energy-bypass," AIAA Paper 2003-0172, 2003.
[18]S. Leonov, V. Bityurin, K. Savelkin, and D. Yarantsev, "Effect of electrical discharge on separation processes and shocks position in supersonic airflow," AIAA Paper 0355, 2002.
[19]S. B. Leonov, D. A. Yarantsev, V. G. Gromov, and A. P. Kuriachy, "Mechanisms of flow control by near-surface electrical discharge generation," AIAA Paper 780, 2005.
[20]K. P. Singh and S. Roy, "Force approximation for a plasma actuator operating in atmospheric air," J. Appl. Phys. **103**(1), 013305 (2008).
[21]C. C. Wang and S. Roy, "Microscale plasma actuators for improved thrust density," J. Appl. Phys. **106**, 013310 (2009).
[22]C. C. Wang and S. Roy, "Numerical simulation of a gas turbine combustor using nanosecond pulsed actuators," AIAA Paper 894, 2013.
[23]C. C. Wang and S. Roy, "Geometry effects of dielectric barrier discharge on a flat surface," AIAA Paper 732, 2011.
[24]E. Moreau, "Airflow control by non-thermal plasma actuators," J. Phys. D: Appl. Phys. **40**(3), 605 (2007).
[25]S. Im, H. Do, and M. A. Cappelli, "Dielectric barrier discharge control of a turbulent boundary layer in a supersonic flow," Appl. Phys. Lett. **97**, 041503 (2010).
[26]T. C. Corke, C. L. Enloe, and S. P. Wilkinson, "Dielectric barrier discharge plasma actuators for flow control," Annu. Rev. Fluid Mech. **42**, 505–529 (2010).
[27]M. Nishihara, K. Takashima, J. Rich, and I. Adamovich, "Mach 5 bow shock control by a nanosecond pulse surface dielectric barrier discharge," Phys. Fluids **23**(6), 066101 (2011).
[28]D. Roupassov, A. Nikipelov, M. Nudnova, and A. Y. Starikovskii, "Flow separation control by plasma actuator with nanosecond pulsed-periodic discharge," AIAA J. **47**(1), 168–185 (2009).
[29]J. S. Shang, R. L. Kimmel, J. A. Menart, and S. T. Surzhikov, "Hypersonic flow control using surface plasma actuator," J. Propul. Power **24**(5), 923–934 (2008).
[30]C. R. Wilke, "A viscosity equation for gas mixtures," J. Chem. Phys. **18**(4), 517–519 (1950).
[31]F. G. Blottner, M. Johnson, and M. Ellis, "Chemically reacting viscous flow program for multi-component gas mixtures," Report SC-RR-70-754, Sandia Labs., Albuquerque, New Mexico, 1971.
[32]W. G. Vincenti and C. H. Kruger, *Introduction to Physical Gas Dynamics* (Wiley, New York, 1965), Vol. 1.
[33]C. Park, *Nonequilibrium Hypersonic Aerothermodynamics* (John Wiley and Sons, New York, 1989).
[34]R. C. Millikan and D. R. White, "Systematics of vibrational relaxation," J. Chem. Phys. **39**(12), 3209–3213 (1963).
[35]A. Bhatia, "Application of parallel time-implicit discontinuous Galerkin finite methods to hypersonic non-equilibrium flow problems," Ph.D. thesis (University of Florida, 2014).
[36]M. R. Visbal, "Strategies for control of transitional and turbulent flows using plasma-based actuators," Int. J. Comput. Fluid Dyn. **24**(7), 237–258 (2010).
[37]D. P. Rizzetta and M. R. Visbal, "Large-eddy simulation of plasma-based turbulent boundary-layer separation control," AIAA J. **48**, 2793–2810 (2010).
[38]J. R. Roth, P. P. Tsai, C. Liu, M. Laroussi, and P. D. Spence, "One Atmosphere, Uniform Glow Discharge Plasma," U.S. Patent #5,414,324, May 1995.
[39]D. M. Schatzman, M. David, and F. O. Thomas, "Turbulent boundary layer separation control with single dielectric barrier discharge plasma actuators," AIAA J. **48**(8), 1620–1634 (2010).
[40]D. Greenblatt, C. Y. Schuele, D. Roman, and C. O. Paschereit, "Dielectric barrier discharge, flow control at very low flight Reynolds numbers," AIAA J. **46**(6), 1528–1541 (2008).
[41]D. P. Rizzetta and M. R. Visbal, "Numerical investigation of plasma based flow control for transitional highly loaded low-pressure turbine," AIAA J. **45**(10), 2554–2564 (2007).
[42]E. Moreau, G. Artana, and G. Touchard, "Surface corona discharge along an insulating flat plate in air applied to electrohydrodynamical airflow control: Electrical properties," Electrostatics **178**, 285–290 (2003).
[43]T. Abe, Y. Takizawa, and S. Sato, "Experimental study for momentum transfer in a dielectric barrier discharge plasma actuator," AIAA J. **46**(9), 2248 (2008).
[44]J. Soni and S. Roy, "Low pressure characterization of dielectric barrier discharge actuators," Appl. Phys. Lett. **102**(11), 112908 (2013).
[45]S. Roy and C.-C. Wang, "Bulk flow modification with horseshoe and serpentine plasma actuators," J. Phys. D: Appl. Phys. **42**, 032004 (2009).
[46]S. Roy and C.-C. Wang, "Numerical Investigation of Three-Dimensional Plasma Actuation for Improving Film Cooling Effectiveness," J. Thermophys. Heat Transfer **27**(3), 489 (2013).
[47]A. Bhatia, S. Roy, and R. Gosse, "Pyrolysis gas flow in thermally ablating media using time-implicit discontinuous Galerkin methods," AIAA Paper 145, 2011.
[48]A. Bhatia, S. Roy, and R. Gosse, "2-D hypersonic non-equilibrium flow simulation using r-p adaptive time-implicit discontinuous Galerkin method," AIAA Paper 0302, 2013.
[49]B. Cockburn and C.-W. Shu, "The Runge–Kutta discontinuous Galerkin method for conservation laws V: Multidimensional systems," J. Comput. Phys. **141**(2), 199–224 (1998).
[50]F. Bassi and S. Rebay, "A high-order accurate discontinuous finite element method for the numerical solution of the compressible Navier–Stokes equations," J. Comput. Phys. **131**(2), 267–279 (1997).
[51]B. Cockburn and C.-W. Shu, "The local discontinuous Galerkin method for time-dependent convection-diffusion systems," SIAM J. Numer. Anal. **35**(6), 2440–2463 (1998).
[52]J. Peraire and P.-O. Persson, "The compact discontinuous Galerkin (CDG) method for elliptic problems," SIAM J. Sci. Comput. **30**(4), 1806–1824 (2008).
[53]P.-O. Persson and J. Peraire, "Newton-GMRES preconditioning for discontinuous Galerkin discretizations of the Navier-Stokes equations," SIAM J. Sci. Comput. **30**(6), 2709–2733 (2008).
[54]N. K. Burgess, "An adaptive discontinuous Galerkin solver for aerodynamic flows," Ph.D. dissertation (University of Wyoming, 2011).

[55]L. Wang, “Techniques for high-order adaptive discontinuous Galerkin discretizations in fluid dynamics,” Ph.D. dissertation (University of Wyoming, 2009).
[56]B. Landmann, “A parallel discontinuous Galerkin code for the Navier-Stokes and Reynolds-averaged Navier-Stokes equations,” Ph.D. dissertation (University of Stuttgart, Germany, 2008).
[57]P. D. Lax, “Weak solutions of nonlinear hyperbolic equations and their numerical computation,” Commun. Pure Appl. Math. **7**(1), 159–193 (1954).
[58]F. Bassi, A. Crivellini, S. Rebay, and M. Savini, “Discontinuous Galerkin solution of the Reynolds-averaged Navier-Stokes and k-w turbulence model equations,” Comput. Fluids **34**(4), 507–540 (2005).
[59]R. D. Falgout and U. M. Yang, “Hypre: A library of high performance preconditioners,” in *Computational Science—ICCS 2002* (Springer, 2002), pp. 632–641.
[60]S. Balay, J. Brown, K. Buschelman, V. Eijkhout, W. Gropp, D. Kaushik, M. Knepley, C. L. McInnes, B. Smith, and H. Zhang, "PETSc Users Manual Revision **3**.4," 2013.
[61]I. Nompelis, T. W. Drayna, and G. Candler, “A parallel unstructured implicit solver for hypersonic reacting flow simulation,” AIAA Paper 4867, 2005.
[62]P. A. Gnoffo, “An upwind-biased, point-implicit relaxation algorithm for viscous, compressible perfect-gas flows,” NASA TP 2953, 1990.